Applied Ocean Research 132 (2023) 103477

Contents lists available at ScienceDirect

Applied Ocean Research

journal homepage: www.elsevier.com/locate/apor

Effect of the implosion of a deep-sea pressure hull on surrounding structures

Yu Wu [a], Ruilong Luo [a], Fang Wang [a], Min Zhao [b,*], Jie Xia [b]

[a] Shanghai Engineering Research Center of Hadal Science and Technology, College of Engineering Science and Technology, Shanghai Ocean University, Shanghai 201306, China
[b] State Key Laboratory of Ocean Engineering, School of Naval Architecture, Civil and Ocean Engineering, Shanghai Jiao Tong University, Shanghai 200240, China

ARTICLE INFO

Keywords:
Deep-sea pressure hull
Submersible
Shock wave
Collapse process

ABSTRACT

A shock wave is generated when a pressure hull implodes in a deep-sea environment, and such an implosion can jeopardise the safety of a deep-sea submersible. However, the damage caused to surrounding structures by the implosion of a high-strength, deep-sea pressure hull has not yet been reported. Therefore, in the present study, the aforementioned aspect was investigated by causing the implosion of a scaled-down submersible pressure hull model in an ultra-high-pressure chamber. A numerical method was developed to predict the multiphase coupling interactions between liquid, gaseous, and solid for two deep-sea pressure hulls. The geometric imperfection of pressure hulls is considered in this method, the first-order linear buckling modal analysis is carried out to simulate initial geometric imperfections. The effect of the shock wave caused by the implosion of one of the pressure hulls on the other pressure hull located nearby was investigated. Moreover, the stress and displacements of characteristic points on the two pressure hulls were examined. The variation in the strain energy of the surrounding pressure hull under pressure hull implosion was also analysed.

1. Introduction

Pressure hulls are integrated into many deep-sea submersibles, such as containers for computers, hydroacoustic communication devices, sounding-side-scan sonar devices, power distribution devices, ballast tanks, high-pressure gas tanks, and pressure-resistant devices (such as underwater lights, cameras, and beacons). The implosion of a certain device in a deep-sea submersible can cause damage to other devices located nearby and negatively affect the safety of the submersible. The investigation of the accident involving the 11,000-m-deep submersible 'Nereus' in 2014 indicated that first, the ceramic ball behind the camera imploded, which caused the generation of a shock wave. This wave caused damage to 1472 ceramic balls with an outer diameter of 10 cm and four large electronic cabins, which led to damage of the entire submersible at a depth of 9990 m.

Many studies have investigated the strength and stability of the pressure hulls of deep-sea submersibles, including the ultimate strength of these hulls when considering their initial defects (Fu et al., 2017; Zhang et al., 2021, 2020). In the early 1940s, a deflection stability theory known as the theoretical foundation of the postbuckling state was proposed (Karman, 1941). A theory for investigating postbuckling behaviours under initial imperfections was proposed, in addition, they proposed a stability theory for describing thin shells on the basis of the theory of elasticity and plasticity for these shells (Koiter, 1970). The theories related to initial defects were generalised for calculating the ultimate load of pressure hull in accordance with the design standards of manned submersibles (Pan and Cui, 2010; Pan and Cui, 2011).

Regarding simulation-based studies, nonlinear buckling analysis of a spherical hull with initial defects was performed (Walter and Ursula, 2002). The nonlinear effects of transverse shear deformation, initial curvature, and stresses acting in the radial and thickness directions were considered to correct the errors in refined two-dimensional linear theories of thin shells (George and Voyiadjis, 2004). A finite-element method (FEM) for buckling analysis of segmented spiral pressure hulls was proposed with different shapes and materials; the results of their study act as a reference in the development of deep-sea stations (Zhang et al., 2022). In one study, the nonlinear buckling of a maraging-steel hemispherical shell under high external pressure was investigated (Zhang et al., 2019). In another study, numerical methods were employed to predict the buckling of egg-shaped pressure hulls (J. Zhang et al., 2018). Furthermore, the nonlinear buckling of hulls with geometric defects was evaluated by developing a modified Risk method for

* Corresponding author.
E-mail address: min.zhao@sjtu.edu.cn (M. Zhao).

https://doi.org/10.1016/j.apor.2023.103477
Received 14 June 2022; Received in revised form 16 December 2022; Accepted 16 January 2023
Available online 22 January 2023

modelling simulation (J. Zhang et al., 2018). The numerical study was performed considering the fluid–structure interaction, strain rate effects, geometric and material non-linearity (Praba and Ramajeyathilagam, 2020), and they studied the localized deformation of thin mild steel plates subjected to underwater explosion (Praba and Ramajeyathilagam, 2022). Moreover, Suresh et al. studied the inelastic dynamic response and microstructure failures of composite hull, the results of the predicted large deformation, puncture of the hull and the microstructural failures were presented (Suresh and Ramajeyathilagam, 2021).

The creep and damage of poly(methyl methacrylate) (PMMA) viewport windows in deep-sea manned submersibles has been investigated using simulation methods. For example, the cyclic creep behaviours and lifetime of conical and spherical viewport windows were predicted by presenting FEM simulations (Li et al., 2021). A method for characterising the material properties of PMMA was developed by using the ABAQUS-UMAT package (Liu et al., 2020). An explicit formula was proposed for calculating the axial displacement of PMMA frustums under various holding times and pressures to provide guidelines on the preliminary design of deep-sea windows (Wang et al., 2021).

Some studies have examined the reliability and fatigue lifetime of pressure hulls. For instance, the weld characteristics of the Ti alloy (TC4) used in spherical pressure shells and the relationship between the plate thickness and welding-heat-affected region of these shells were investigated (Yu et al., 2022). The effects of the ratio of intermittent loading time were evaluated to stress on the dwell fatigue behaviours of a Ti alloy (Ti–6Al–4V) (Sun et al., 2021). In (Lee and Park, 2019), the collapse behaviours of deep-sea pressure hulls were investigated to predict their cylinder thickness under the ultimate collapse load, and a crack growth model was employed to predict the fatigue lifetime of these hulls. A modified crack growth rate model was proposed for a small time scale by considering the effects of overloading as well as load-sustaining and stress–strain constraints (Wang et al., 2022). Fatigue crack growth rates were predicted under different load ratios by using various fatigue crack growth models (Li et al., 2022). In (Sun et al., 2021), the dwell fatigue behaviours of a Ti alloy (Ti–6Al–4V) were investigated by considering the effects of the ratio of intermittent loading time to stress. The model proposed in (Wang et al., 2020) for dwell fatigue crack growth involved adjustment of the plastic zone of a crack tip under loading variation; the single overload and dwell time factors were also considered in this model.

A deep-sea pressure hull implodes when the water pressure exceeds the ultimate strength of the hull. This implosion causes the conversion of hydrostatic pressure into fluid kinetic energy, which results in the generation of a shock wave that damages surrounding structures. A series of numerical simulation studies were conducted during the 1980s and 1990s to analyse the damage effect of an imploding pressure hull in an ultra-high-pressure chamber (Zhu and Luo, 1983). The Unmanned Undersea Vehicle Program Plan published by the US Navy in 2004 requires the effects of pressure hull implosion to be considered during submarine design (Turner, 2004). In 2007, the US Warfare center proposed that the external equipment carried by a submarine might implode and that this may induce shock waves that damage the submarine hull; their proposal was validated through an experiment (Kent, 2008). Implosion tests for a photomultiplier tube were conducted in a 0.69-MPa hydrostatic pressure tank and measured the pressure during the implosion process (Diwan and Dolph, 2012). An implosion test of an underwater metal cylindrical shell was conducted in a pressure tank and they studied the effects of the length, diameter, and thickness of the shell on the generated shock waves (Gish and Wierzbicki, 2015). A series of underwater implosion tests were conducted for thin-walled aluminium alloy tubes and recorded the states of the tubes after implosion (Turner and Ambrico, 2013). On the basis of theoretical and experimental research, the vibration frequency of a structure decreases with an increase was found in the static pressure of the surrounding water during the implosion of an aluminium alloy cylindrical shell. Such a decrease in vibration frequency leads to a decrease in the stiffness of the structure (Gupta et al., 2016). The implosion of a single stainless-steel spherical shell and multiple stainless-steel spherical shells were studied through theoretical analysis, FEM simulation, and experimental testing (Ferris, 2017). The relationship between water hammer and shock wave impact was investigated in the underwater implosion of a thin-walled aluminium alloy cylindrical shell (Matos et al., 2018). In Sik et al. (2020), the dynamic buckling and collapse response of a pressure vessel in deep sea were predicted by considering the effects of initial hydrostatic pressure and solid–fluid interactions.

In summary, previous simulations and analyses of spherical pressure hulls have been based on the static load of the seawater environment, and a safety factor has been used to analyse the safety of spherical pressure hull designs. However, the effect of the implosion of a deep-sea pressure hull on surrounding structures (particularly another pressure hull) has not yet been determined. The collapse process of a pressure hull involves strong and rapid coupling interactions between fluid and solid phases, extremely high pressure, and high nonlinearity. Accordingly, in this study, a model that considers the multiphase coupling processes between liquid, solid, and gaseous phases was developed to predict the effect of the implosion of one pressure hull on another pressure hull (i.e., the damage to the other hull). The stresses and displacements at characteristic points on pressure hulls were examined, and the strain energy of a pressure hull after implosion of a nearby pressure hull was analysed.

2. Experimental testing

A spherical hull was assembled from two coupled hemispherical hulls through butt-welding under tungsten inert gas, and the hull's surface was ground and polished. The geometric details of the hull, such as its bulk diameter and thickness, were measured to enable construction of our proposed model. The thickness of the hull was measured by using an ultrasonic thickness gauge (Olympus 38DLPLUS, Boston, USA) with a Panametrics NITD792 probe. As displayed in Fig. 1, each grid of the measurement mesh was assumed to cover a latitude and longitude of 15°

By using the measured thickness and bulk diameter of the pressure hull, its collapse load was calculated, and this load was employed to determine the approximate pressure range suitable for testing. The collapse load equation proposed in (J. Zhang et al., 2018) is as follows:

$$P_u = k_p k_{imp} \frac{2Et}{R(1-\mu^2)} \left[\sqrt{\frac{(1-\mu^2)}{3}} \ \frac{t}{R} - \frac{\mu t^2}{2R^2} \right] \tag{1}$$

where

$$k_p = 8.92 \times 10^{-6} \sigma_s \left(\frac{t}{R}\right)^{-0.986}$$

$$k_{imp} = \begin{cases} k_1 \dfrac{t}{R} + k_2 & \left(0.025 < \dfrac{t}{R} < 0.045\right) \\ (0.045k_1 + 0.055k_3 + k_2 + k_4)/2 & \left(0.045 < \dfrac{t}{R} < 0.055\right) \\ k_3 \dfrac{t}{R} + k_4 & \left(0.055 < \dfrac{t}{R} < 0.080\right) \end{cases}$$

In this equation, P_u is the collapse load of a spherical pressure hull; E is the Young's modulus of the hull; σ_s is the yield strength of the hull; μ is the Poisson's ratio of the hull; R and t are the mean radius and thickness of hull, respectively; and k_1, k_2, k_3, and k_4 are imperfection coefficients.

The prepared spherical pressure hull was placed in a 140-MPa ultra-high-pressure chamber. Strain measurements were performed on the outer walls of the upper and lower hemispheres of the spherical hull. Three 16-core, high-voltage watertight cable joints and 17 strain gauge measurement points were selected. To reduce the impact force caused by damage to the pressure hull, a water bag was placed in its cabin; the

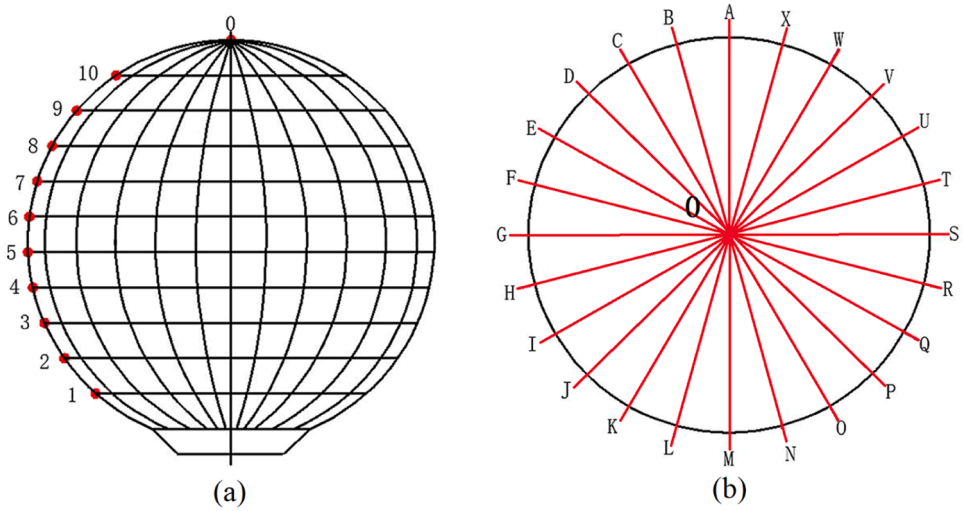

Fig. 1. Measurement grids for the model sphere: (a) front view and (b) top view.

water bag's volume was approximately 60% of the hull's volume. Subsequently, the tightness of the hull was checked. Finally, the spherical hull was subjected to a water pressure test in the ultra-high-pressure chamber. A photograph of this chamber is displayed in Fig. 2.

The prepared spherical pressure hull, which had an inner diameter of 500 mm and an outer diameter of 518 mm, collapsed during the pressure test. The hull was made of Ti–6Al–4V and was a scaled-down version of the pressure hull of a manned submersible with a 660-mm-diameter cover. The pressure in the chamber was increased by 5×10^6 Pa every 3 min during the pressure test, and the prepared hull collapsed at a load of 51×10^6 Pa. Photographs of the destroyed spherical hull and its fragments are shown in Fig. 3. The spherical hull was severely damaged and broke into several pieces from the reinforced forgings at its opening. The reinforcement forging with a hole was completely separated from the spherical hull, and the three broken fragments displayed in Fig. 3(c) were located between the equatorial weld and the reinforcement forging weld. These fragments contained materials of the spherical hull and welds, which indicated that cracking originated near the aforementioned two welds.

3. Effect of pressure hull implosion on surrounding structures

The results of explicit dynamic analysis indicate that a cylindrical specimen shrinks under tension, which is in agreement with the experiment results [38]. Mesh convergence analysis is conducted. In Fig. 4, cases A–E denote the stress–strain relationships for mesh sizes of 0.0015, 0.002, 0.0025, 0.003, and 0.0035 m, respectively. These mesh sizes correspond to 6364, 2904, 1664, 1144, and 760 meshes, respectively, and computing times of 9.2, 4.2, 2.4, 1.65, and 1.1 min, respectively. Compared with the experimental data, the predicted data tended to converge more when the mesh was finer. The similarity between the predicted and experimental fracture strain was approximately 98% for case C, and the stress–strain curve for case C was obtained with acceptable accuracy and computational cost (Wu et al., 2022); thus, this curve was sufficiently accurate for modelling the strain–stress relationship in the present study.

The assumed boundary condition for three-point constraints is illustrated in Fig. 5(a). To determine the failure mode of the prepared pressure hull, its geometric imperfections were considered. A pressure of 1 MPa was applied to the outer surface of the pressure hull, and the first-order mode was used to determine the buckling mode of the pressure hull [Fig. 5(b)]. Geometric imperfections were introduced as follows.

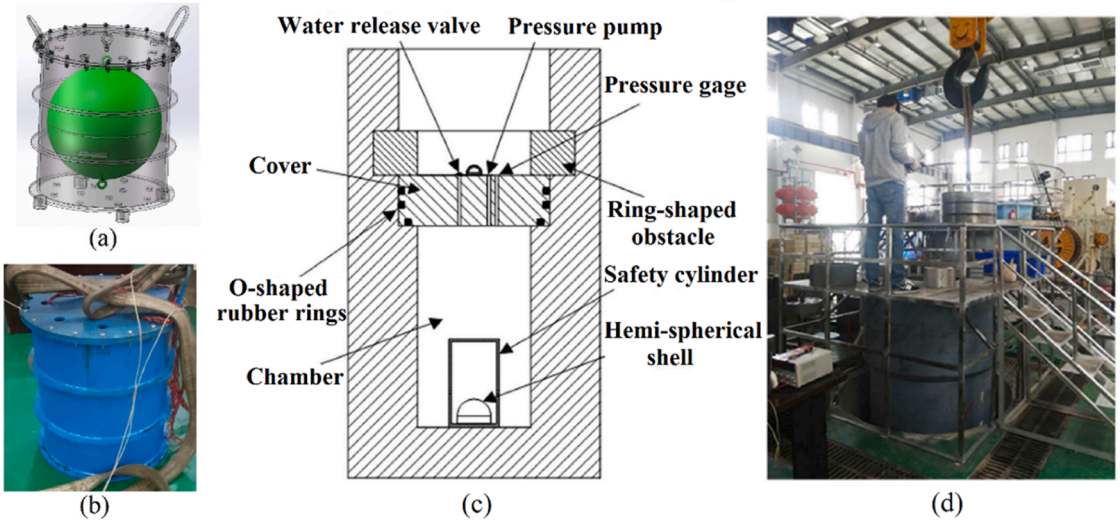

Fig. 2. Experimental setup: (a) schematic and (b) photograph of the protective cover of the pressure chamber, and (c) schematic and (d) photograph of the adopted pressure chamber.

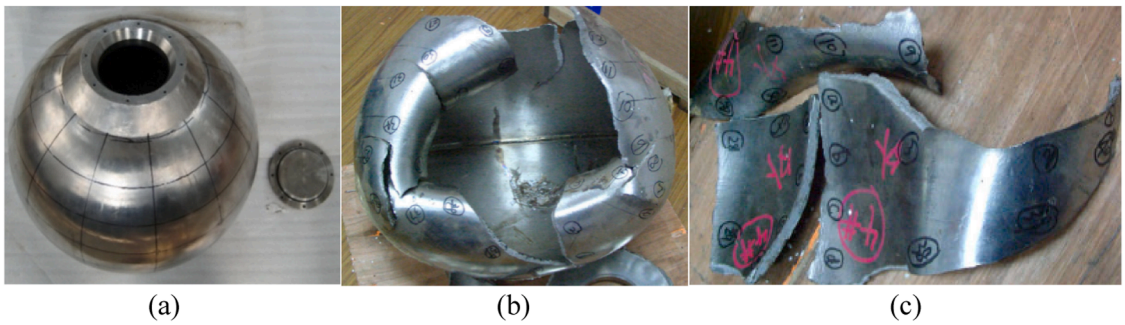

Fig. 3. Photographs of the prepared spherical pressure hull before and after its implosion: (a) prototype before its collapse, (b) collapsed prototype, and (c) fragments of the pressure hull in the pressure chamber.

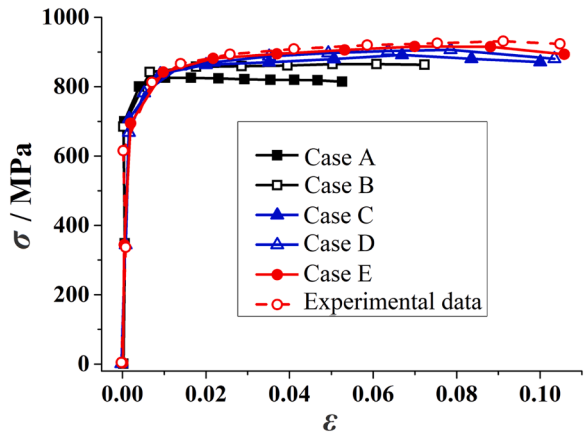

Fig. 4. Stress–strain curves for various mesh sizes (cases A–E: mesh sizes of 0.0015, 0.002, 0.0025, 0.003, and 0.0035 m, respectively).

First, the first-order buckling mode of the fabricated pressure hull was determined through buckling analysis. The keyword had to be modified (the statement *node file, global = yes U, was inserted before *End Step). Second, the buckling mode of the prepared pressure hull was copied, the statement *node file was deleted, and nonlinear analysis was conducted. Subsequently, the keyword was modified again. The statement *IMPERFECTION, FILE = Job-2, step = 1 1, 0.026 was inserted after the statement *Boundary, where 1 and 0.026 represent the mode and coefficient, respectively. In the buckling analysis, the displacement of the initial defect was equal to the product of the coefficient and maximum displacement.

The Abaqus software is used in finite-element model analysis, and complex nonlinear problems can be solved by using the built-in solver of this software. Abaqus can be used to analyse not only the basic physical field but also the fluid–solid coupling field. A theoretical formula for calculating underwater implosion intensity is built into this software. It can use not only use the coupled Euler–Lagrange algorithm and FEM to calculate the response of a structure under underwater implosion but also an acoustic structure coupling algorithm to simulate the underwater explosion impact. Therefore, Abaqus is efficient for analysing the effects of an implosion on nearby structures.

The sectional view of the finite-element model developed in this study is shown in Fig. 6. A multiphase collapse model was developed to predict the complex collapse behaviours of a spherical hull by considering the coupling interactions between fluid (liquid and gas) and solid phases. The discrete Lagrangian method was used for numerical calculations, and a Eulerian mesh and Lagrangian mesh were employed to describe the fluid region (liquid and gaseous phases) and solid region (pressure hull), respectively. All Eulerian elements were initially defined as 'virtual materials', which can be defined by initial conditions to fill the Eulerian elements with water and air (the material properties of water and air are defined in Eulerian sections). The initial shape of the Eulerian material was achieved by selectively filling the material. The material of the mesh was determined by calculating the volume fraction. The material was filled until the volume fraction reached 1, and the remaining material was ignored. Initial conditions were defined at the beginning of the analysis, the material deformation depended on the defined load, and the volume fraction was recalculated. The specific steps were as follows: *INITIALCONDITIONS, TYPE = VOLUME-FRACTION; Abaqus/CAE: Load: Create Predefined Field->; Step: Initial-

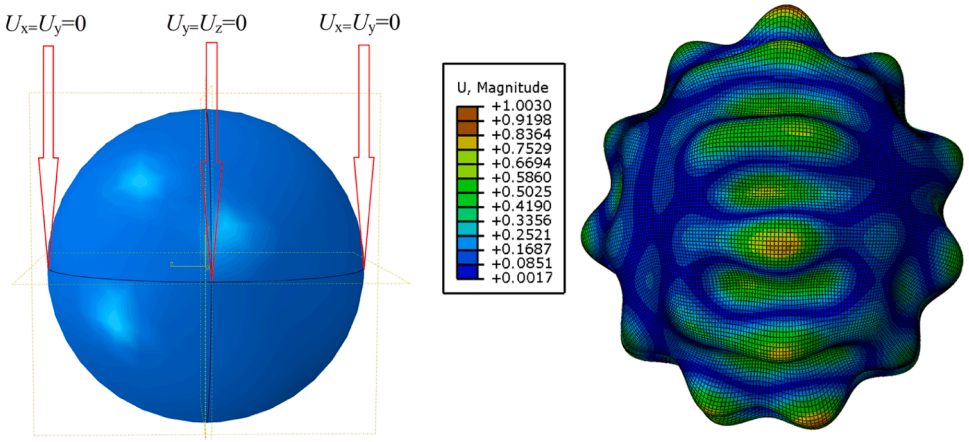

Fig. 5. Three-point constraint and linear buckling mode.

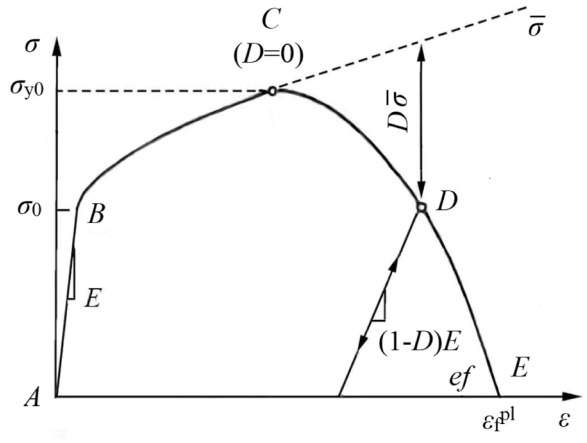

Fig. 6. Stress–strain curve of the metallic pressure hull.

>Category: Other->Material Assignment.

The following Eulerian boundary conditions were assumed for the developed model: the external hydrostatic pressure defines the pressure field at the boundary of the Eulerian domain; and a shock wave without reflection forms at the boundary of an infinite Eulerian domain. If no shear stress exists at the Eulerian–Lagrangian contact interface and the friction coefficient between the contact surfaces is 0, then 'hard contact' is assumed to be the general contact property. When the gap between these surfaces becomes 0, they are considered to be in contact, and contact constraints are imposed on the corresponding nodes. When the contact pressure between the contact surfaces becomes 0 or negative, the contact interfaces are separated, and the contact constraints are released. The linear *Us*–*Up* Hugoniot equation of state (EOS) is used for water and air model:

$$p = \frac{\rho_0 c_0^2 \eta}{(1-s\eta)^2}\left(1-\frac{\Gamma_0 \eta}{2}\right) + \Gamma_0 \rho_0 E_m \tag{2}$$

where Γ is the Grignard Nessen ratio ($\Gamma = \Gamma_0 \frac{\rho_0}{\rho}$, Γ_0 is the Grignard Nessen constant of the material), $\rho_0$is the reference density, c_0 is the linear impact velocity of the material, s is the slope coefficient of the *Us*–*Up* curve, and $\eta = 1 - \rho_0/\rho$ is the nominal volume compression strain.

Water and air are regarded as linear materials, and water and air flowing at low speed are Newtonian fluids whose linear impact velocity and viscosity are only related to the temperature. The linear impact velocity and dynamic viscosity of water and air at 4 °C are selected in model. The density, EOS, viscosity, and elasticity of the materials (water, air, and metallic pressure hull) of the developed model are listed in Table 1.

The stress–strain curve of the metallic pressure hull is displayed in Fig. 6.

In Fig. 6, segment AB represents elastic deformation, point B is the yield point, segment BC represents plastic deformation, point C is the damage initiation point, segment CE represents the damage process, and point E is the failure point.

The metal ductility fracture criteria in Abaqus describe the damage stage CE. The equivalent fracture strain at damage initiation (denoted ε_D^{pl}), stress triaxiality (denoted η; $\eta = -p/q$, where p is the compressive stress and q is the Mises stress), and equivalent plastic strain rate (denoted ε^{pl}) are required.

The metal is damaged when the following equation is satisfied:

$$\int \frac{d\varepsilon^{pl}}{\varepsilon_D^{pl}(\eta, \varepsilon^{pl})} = 1 \tag{3}$$

The damage variable w_D is assumed to increase with the degree of plastic deformation and can be expressed as follows:

$$\Delta\omega_D = \frac{\Delta\varepsilon^{pl}}{\varepsilon_D^{pl}(\eta, \varepsilon^{pl})} \geq 1 \tag{4}$$

As displayed in Fig. 7, two titanium alloy pressure hulls (pressure hulls I and II) are considered for simulation. Pressure hull II is assumed to have an inner diameter of 500 mm and an outer diameter of 518 mm (same as the experimental sample), whereas pressure hull I is assumed to have an inner diameter of 494 mm and an outer diameter of 518 mm. Pressure hull I is 3 mm thicker than pressure hull II, and the distance between the two hulls is assumed to be 50 mm.

The collapse loads for the aforementioned pressure hulls are different because of their different thicknesses. When the pressure is increased by 5×10^6 Pa every 3 min, pressure hull II collapses at 52×10^6 Pa (error of 1.9% with respect to the experimental collapse load of 51×10^6 Pa). As show in Fig. 8. In contrast to the damage process for the experimental pressure hull, which had an access hole, the damage of pressure hull II begins in its middle region, spreads throughout the hull under high external pressure, and results in the generation of large fragments. Pressure hull II absorbs energy continuously during static loading, and most of this energy is stored as elastic energy. The energy that is dissipated during the damage of pressure hull II accounts for a small proportion of the total energy. When the load reaches the ultimate bearing capacity of pressure hull II, its elastic energy is suddenly released in its weak area, which results in the generation of fragments with high flow kinetic energy that impact and damage nearby structures.

As illustrated in Fig. 8, when the load reaches 52×10^6 Pa, pressure hull I does not collapse but is damaged by the shock wave generated by the implosion of pressure hull II (Fig. 9).

The maximum stress acting on pressure hull I increases from 5.041×10^8 to 7.601×10^8 Pa during the implosion process, and the minimum stress is 6.165×10^5, 6.257×10^5, 1.242×10^6, 8.251×10^6, 4.597×10^6, and 3.299×10^6 Pa at 1.0051×10^{-5}, 3.0052×10^{-5}, 5.0052×10^{-5}, 1.8006×10^{-4}, 6.8005×10^{-4}, and 9.6005×10^{-4} s, respectively.

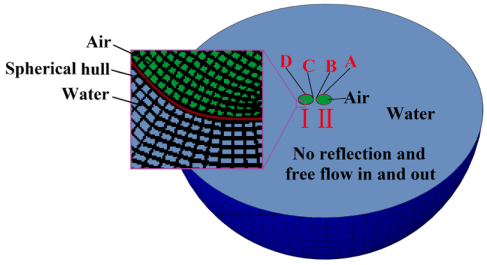

Fig. 7. Sectional view of the simulation domain in the FEM model.

Table 1
Properties of the materials of the developed model.

Materials	Density kg/m^3	Equation of state Us-Up Hugoniot			Viscosity Newtonian Pa•s	Elasticity	
		c_0	s	Γ_0		Young's modulus N/m^2	Poisson's ratio
Air	1.293	283	0	0	1.73×10^{-5}	–	–
Water	1000	1480	0	0	0.001	–	–
Pressure hull	4430	–	–	–	–	1.08×10^{11}	0.3

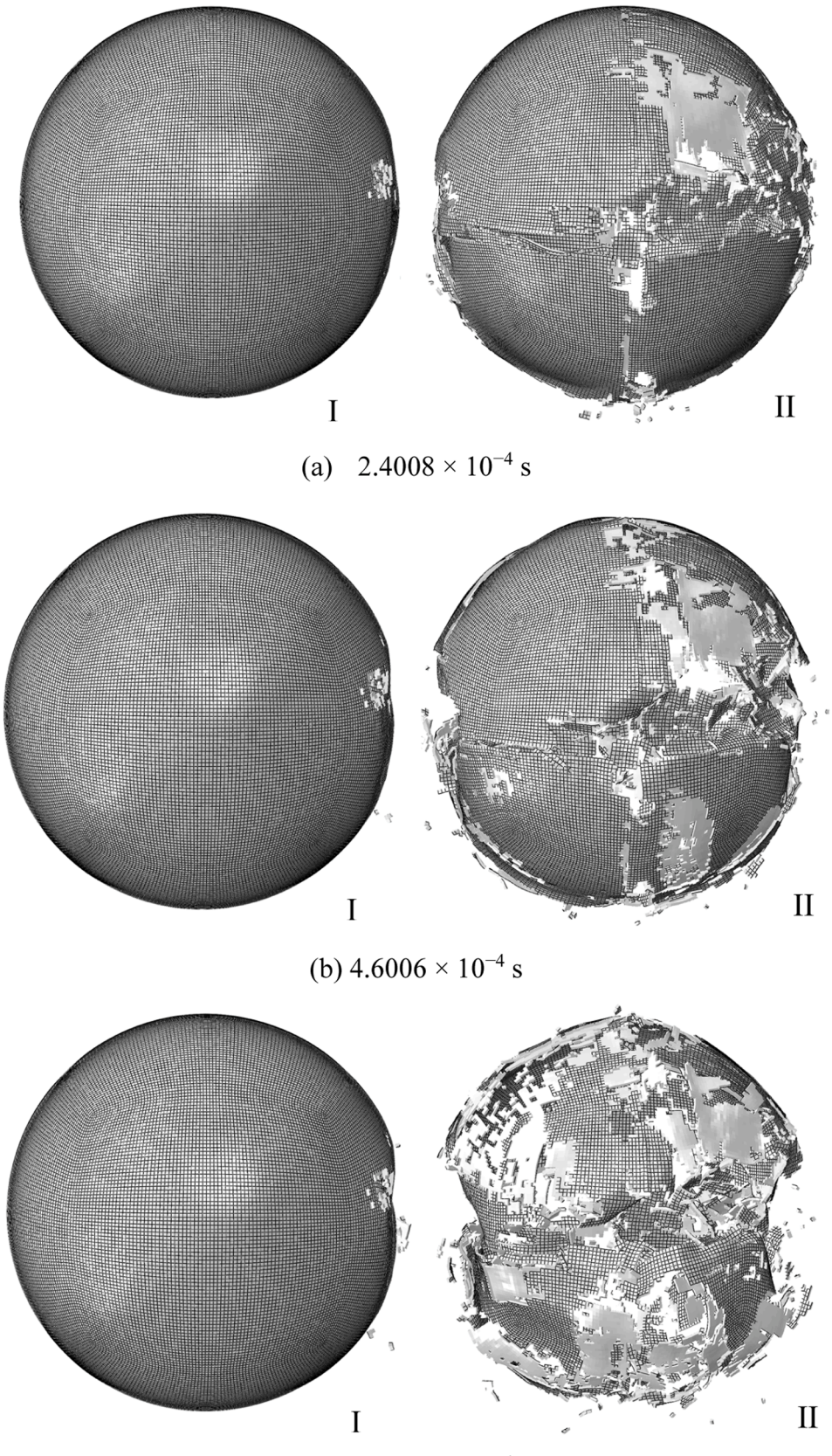

Fig. 8. Collapse processes of spherical hulls I and II.

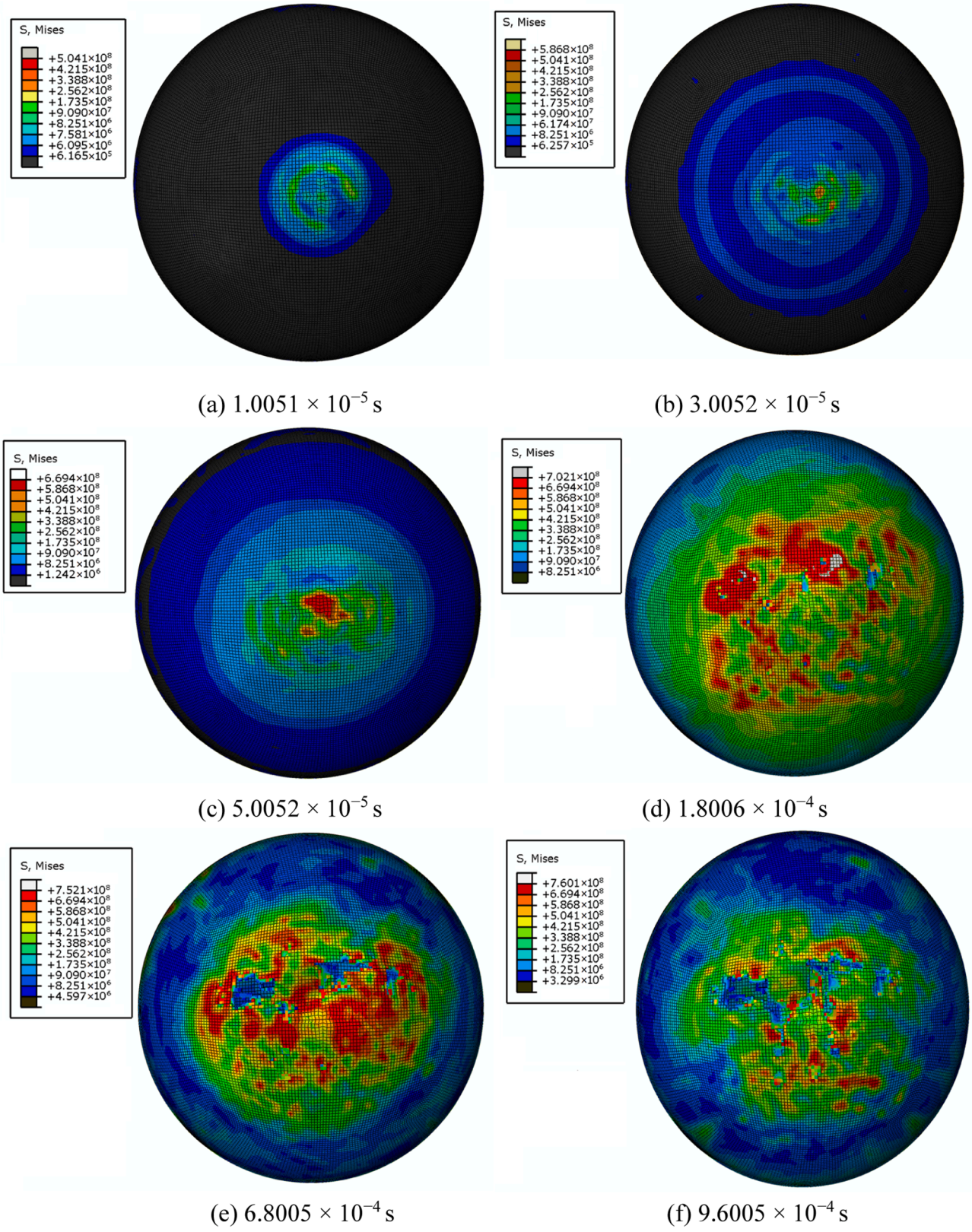

Fig. 9. Damage of and stress acting on pressure hull I after the collapse of pressure hull II.

Because of the shock wave generated by the implosion of pressure hull II, the stress acting on pressure hull I increases from the minimum stress. Subsequently, the pressure hull is damaged, and the stress acting on it reaches the hull's maximum value. The stress then decreases with increasing damage of pressure hull I.

Fig. 10 displays the displacements of pressure hull I under the shock wave generated by the implosion of pressure hull II. The maximum displacements of pressure hull I at 6.8005×10^{-4} and 9.6005×10^{-4} s are 2.067×10^{-2} and 2.876×10^{-2} m, respectively. The whole surface of pressure hull II is damaged, and the damaged surface of pressure hull

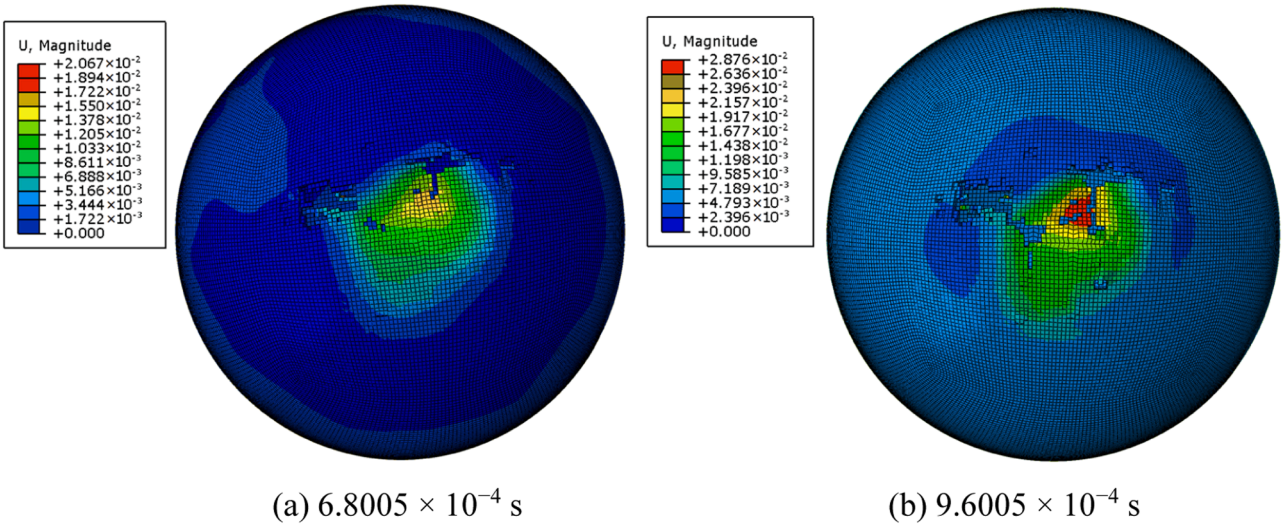

Fig. 10. Displacements of pressure hull I under the shock wave generated by the implosion of pressure hull II.

1 is about 0.05 m^2.

Illustrated in Fig. 11(a) and 11(b), points A and B on pressure hull II and points C and D on pressure hull I are considered characteristic points. Points B and C are located at the equators of the hulls, whereas points A and D are extreme points on the northern hemispheres of the hulls. The stress and displacement variations over time for these points are displayed in Figs. 11 and 12, respectively.

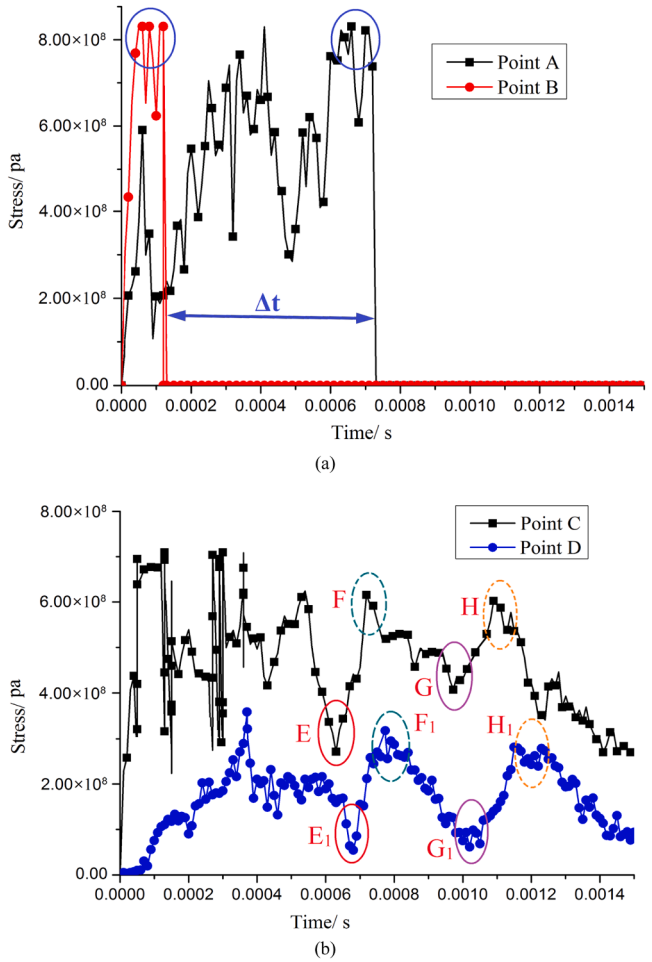

Fig. 11. Stress variation over time for (a) points A and B on pressure hull II and (b) points C and D on pressure hull I.

As displayed in Fig. 11(a), the magnitudes and trends of the stress acting on points A and B are the same. The stress increases from 0 to 8.302 × 10^8 Pa and then decreases to 0 Pa for pressure hull II. However, the stress variation over time at point B (the equatorial point) has a delay of 0.0006 s with respect to that at point A (the extreme point in the northern hemisphere). For a spherical pressure hull, stress concentration and deformation first occur at the equator and then lead to the pressure hull collapsing at the equator. The stress and deformation then propagate to the top and bottom sides, following which the entire pressure hull collapses.

As depicted in Fig. 11(b), the stress at equatorial point C increases from 0 Pa to between 3 × 10^8 and 7.5 × 10^8 Pa, then reduces to 4.6 × 10^8 Pa after 0.0007 s, and finally reduces to 0 Pa. The stress trend at extreme point D is similar to that at point C. The stress at point D first increases from 0 to 3.7 × 10^8 Pa, then decreases to 5.30 × 10^7 Pa after 0.0008 s, and finally decreases to 0 Pa. In summary, the stress at extreme point D is 3.0 × 10^8 to 3.5 × 10^8 Pa higher than that at equatorial point C. Moreover, the stress trend at point D exhibits a delay of 0.0001 s with respect to that at point C. Therefore, pressure hull I is damaged at its equator rather than at its extreme points.

As shown in Fig. 12(a), the displacements of points A and D increase gradually over time. The largest displacement of 0.66 m is observed for point B at 0.0015 s, and the displacements of points A, C, and D are 0.057, 0.025, and 0.005 m, respectively. The simulation results indicate that pressure hull I is damaged by the shock wave generated by the collapse of pressure hull II. Notably, the overall displacement of pressure hull I is small; however, the strain energy acting on it increases sharply after pressure hull II collapses [Fig. 12(b)]. The fluctuation in the strain energy–time curve of pressure hull I indicates the development and recovery of elastic deformation of this pressure hull. When the strain energy does not decrease further, pressure hull I exhibits fully plastic deformation. The maximum strain energy density for this pressure hull occurs at 0.00083 s. The relationship between distance from pressure hull II and damage was investigated for pressure hull I. Fig. 13 indicates that the stress of pressure hull I decreases rapidly for distances longer than 150 mm from pressure hull II, and the stress is close to 0 when this distance is 250 mm (i.e., pressure hull I is not damaged at this distance).

4. Conclusion

In this study, a scaled-down pressure hull model of a manned submersible was placed in an ultra-high-pressure chamber to conduct a pressure experiment. The pressure in the chamber was increased by 5 ×

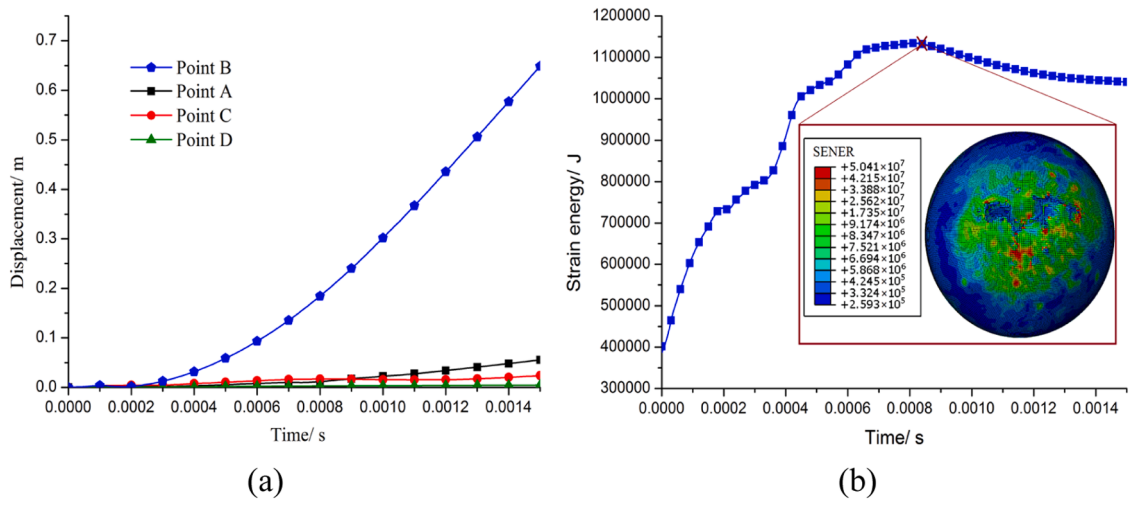

Fig. 12. Displacements and strain energy variations at different points on pressure hulls I and II: (a) displacement variation with time at points A–D and (b) strain energy variation with time of pressure hull I.

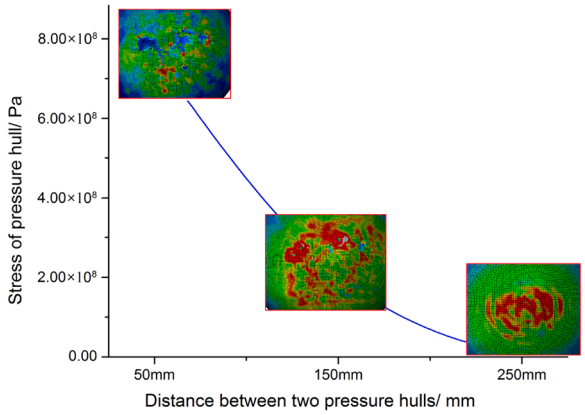

Fig. 13. Relationship between the distance from pressure hull II and damage to pressure hull I.

10^6 Pa every 3 min, and the aforementioned pressure hull collapsed at a load of 51 $\times$ 10^6 Pa. A numerical model was developed to predict the multiphase coupling interactions in the implosion of a spherical pressure hull. Three-point constraints and geometric imperfections were incorporated into this model, and the first-order linear buckling modal analysis was used to determine the buckling mode of a spherical pressure hull. The dynamic collapse and destruction of a spherical pressure hull were examined through an experiment and simulations. The effect of the shock wave generated by pressure hull collapse on a surrounding pressure hull was also investigated. The stress acting on and displacement of characteristic points on the surrounding pressure hull were examined. The magnitude and trend of the stress acting on an equatorial point and extreme point on the collapsed pressure hull were identical (ranging from 0 to 8.302 $\times$ 10^8 Pa). However, the stress variation over time at the equatorial point exhibited a delay of 0.0006 s with respect to that at the extreme point. For the surrounding pressure hull, the stress at an extreme point was 3.0 $\times$ 10^8 to 3.5 $\times$ 10^8 Pa higher than that at an equatorial point, and the stress variation over time at the extreme point exhibited a delay of 0.0001 s with respect to that at the equatorial point. The strain energy of the surrounding pressure hull increased sharply after the collapse of the other pressure hull. This study can act as a reference in examinations of the effect of the implosion of deep-sea pressure hulls on surrounding structures.

Author statement

Yu Wu: Original draft preparation
Ruilong Luo: Modelling, Formal analysis
Fang Wang: Conceptualization, Methodology
Min Zhao: Review & editing
Jie Xia: Modelling, Formal analysis
All authors have read and agreed to the published version of the manuscript.

Declaration of Competing Interest

The authors declare that they have no known competing financial interests or personal relationships that could have appeared to influence the work reported in this paper.

Data availability

No data was used for the research described in the article.

Acknowledgement

This work is supported by the National Natural Science Foundation of China (Grant No.U2067220, No.51779139, No.52101320 and No.52071203), the Young Talent Project of China National Nuclear Corporation and the Top Young Talents of Ten Thousand Talents Plan; the support of Fishery Engineering and Equipment Innovation Team of Shanghai High-level Local University and the authors would like to express their gratitude for the support of Fishery Engineering and Equipment Innovation Team of Shanghai High-level Local University.

References

Diwan, M., Dolph, J., 2012. Underwater implosions of large format photo- multiplier tubes. Nucl. Instrum. Methods Phys. Res. 670 (3), 61–67.
Ferris, E.G., 2017. A computational and experimental study of the underwater implosion of single and multiple metallic spherical shells. Massach. Inst. Technol. 65, 22–29.
Fu, P.F., Mao, Z.Y., Tang, Z.Y., Li, K., Wang, X.C., Zuo, C.J., 2017. Microstructures and properties of TC4 ELI alloy with horizontal EBW for submersible manned cabin. Appl. Ocean Res. 68, 237–243.
George, Z., Voyiadjis, P.W., 2004. A refined theory for thick spherical shells. Int. J. Solids Struct. 41, 3747–3769.
Gish, L.A., Wierzbicki, T., 2015. Estimation of the underwater implosion pulse from cylindrical metal shells. Int. J. Impact Eng. 77, 166–175.
Gupta, S., Matos, H., LeBlanc, J.M., 2016. Shock initiated instabilities in underwater cylindrical structures. J. Mech. Phys. Solids 95, 188–212.

Karman, T.V., 1941. The buckling of thin cylindrical shells under axial compression. J. Aeronaut. Sci. 8, 303–312.
Kent, T.R., 2008. Implosion research. Sea Frame 112 (4), 263–269.
Koiter, W.T., 1970. The stability of elastic equilibrium. Stab. Elast. Equilib. 1–10.
Lee, J., Park, B., 2019. The analysis of collapse load of thick pressure cylinder under external hydrostatic pressure. J. Soc. Naval Archit. Korea 56 (2), 175–186.
Li, Y.Z., Huang, X.Y., Wang, K., Bai, X., Li, Y.Q., Zhang, S.X., Bian, C., Bian, C.C., Gao, L. Q., Wu, L., 2022. Research on fatigue crack growth behavior: experimental and prediction method of titanium alloy. Int. J. Mod. Phys. B 36 (12N13), 2240071.
Li, J.X., Liu, P.F., Tong, X.Y., 2021. A simplified method for studying cyclic creep behaviors of deep-sea manned submersible viewport windows. Int. J. Press. Vess. Pip. 194, 104565.
Liu, P.F., Li, J.X., Wang, S.B., Leng, J.X., 2020. Finite element analysis of viscoelastic creep behaviors of deep-sea manned submersible viewport windows. Int. J. Press. Vess. Pip. 188, 104218.
Matos, H., Gupta, S., Shukla, A., 2018. Structural instability and water hammer signatures from shock-initiated implosions in confining environments. Mech. Mater. 116, 169–179.
Pan, B.B., Cui, W.C., 2010. An overview of buckling and ultimate strength of spherical pressure hull under external pressure. Mar. Struct. 23 (3), 227–240.
Pan, B.B., Cui, W.C., 2011. A comparison of different rules for the spherical pressure hull of deep manned submersibles. J. Ship Mech. 15 (3), 276–285.
Praba, R.P.S., Ramajeyathilagam, K., 2020. Numerical investigations on the large deformation behaviour of ring stiffened cylindrical shell subjected to underwater. Appl. Ocean Res. 101, 102262.
Praba, R.P.S., Ramajeyathilagam, K., 2022. Microstructural damage and response of stiffened composite submersible pressure hull subjected to underwater explosion. Ships Offshore Struct. https://doi.org/10.1080/17445302.2022.2107308.
Sik, N.I., Sang-rai, C., Sik, C.Y., 2020. Dynamic stability assessment of pressure hull in deep sea against implosion pressure pulse. J. Soc. Naval Archit. Korea 57 (4), 198–206.
Sun, C.Q., Li, Y.Q., Xu, K.L., Xu, B.T., 2021. Effects of intermittent loading time and stress ratio on dwell fatigue behavior of titanium alloy Ti-6Al-4V ELI used in deep-sea submersibles. J. Mater. Sci. Technol. 77, 223–236.
Suresh, C., Ramajeyathilagam, K., 2021. Large deformation behaviour of thin mild steel rectangular plates subjected to underwater explosion loading under air and water backed conditions. Appl. Ocean Res. 114, 102780.
Turner, S.E., 2004. Small-scale implosion testing of glass and aluminum cylinders, NUWC-NPT technical memorandum 04-061, Naval Undersea Warfare Center Division.
Turner, S.E., Ambrico, J.M., 2013. Underwater implosion of cylindrical metal tubes. J. Appl. Mech. 80 (1), 819–833.
Wang, F., Wang, M.Q., Wang, W.W., Yang, L., Zhang, X.Z., 2021. Time-dependent axial displacement of PMMA frustums designed for deep-sea manned cabin based on finite element analysis. Ships Offshore Struct. 16 (8), 827–837.
Wang, F., Zhang, X.Z., Kong, P.P., Zhang, J.F., Luo, R.L., Zhang, J., Wang, Y.M., 2022. An improved small-time-scale crack growth rate model considering overloading and load-sustaining effects for deep-sea pressure hulls. Ocean Eng. 247, 110361.
Wang, K., Wu, L., Li, Y.Z., Sun, X.P., 2020. Study on the overload and dwell-Fatigue property of titanium alloy in manned deep submersible. China Ocean Eng. 34 (5), 738–745.
Walter, W., Ursula, A., 2002. Buckling behavior of imperfect spherical shells. Int. J. Non Linear Mech. 37 (4–5), 569–604.
Wu, Y., Ding, J., Wang, F., Sun, Z.Z., Zhao, M., Wang, Y.M., 2022. Research on the quasi-static collapse and instantaneous implosion of the deep-sea spherical pressure hull. Mar. Struct. 83, 103191.
Yu, C.L., Guo, Q.B., Gong, X.B., Yang, Y.F., Zhang, J., 2022. Fatigue life assessment of pressure hull of deep-sea submergence vehicle. Ocean Eng. 245, 110528.
Zhang, J., Zhang, M., Pan, B.B., 2018a. Elastic-plastic buckling of deep sea spherical pressure hulls. Mar. Struct. 57, 38–51.
Zhang, J., Zhang, Y.W., Jiang, Z., 2019. Experimental and numerical studies on the buckling of the hemispherical shells made of maraging steel subjected to extremely high external pressure. Int. J. Pressure Vess. Pip. 172, 56–64.
Zhang, J., Wang, R., Wu, W.W., 2022. Numerical and experimental buckling of segmented spiral pressure hulls. J. Mech. Sci. Technol. 36 (4), 1799–1807.
Zhang, J., Wang, X., Tang, W.X., Wang, F., Yin, B.j., 2020. Experimental and numerical buckling analysis of toroidal shell segments under uniform external pressure. Thin-Walled Struct. 150, 106689.
Zhang, J., Zhu, Z.Y., Wang, F., Zhao, X.L., Zhu, Y.M., 2021. Buckling of double-layer and single-layer stainless steel cylinders under external pressure. Thin-Walled Struct. 161, 107485.
Zhang, J., Wang, M.L., Tang, W.X., 2018b. Effect of thickness on the buckling strength of egg-shaped pressure hulls. Ships Offshore Struct. 13 (4), 375–384.
Zhang, J., Zhang, M., Cui, W.C., Tang, W.X., Wang, F., Pan, B.B., 2018c. Elastic-plastic buckling of deep sea spherical pressure hulls. Mar. Struct. 57, 38–51.
Zhu, J.M., Luo, M.L., 1983. Theoretical analysis and prediction of implosion during a high pressure test in GUSI-A1. GKSS.